Incorporating Pyrrolic and Pyridinic Nitrogen into a Porous Carbon made from C_{60} Molecules to Obtain Superior Energy Storage

Ziqi Tan, Kun Ni, Guanxiong Chen, Wencong Zeng, Zhuchen Tao, Mujtaba Ikram, Qiubo Zhang, Huijuan Wang, Litao Sun, Xianjun Zhu, Xiaojun Wu, Hengxing Ji, Rodney S. Ruoff, and Yanwu Zhu**

Nanostructures made of sp^2-hybridized carbon atoms such as fullerene,[1] carbon nanotubes (CNTs),[2] and graphene[3] have been the focus of carbon materials research in reversible electrochemical energy storage because of their excellent electric conductivity, chemical and mechanical stability, and the tailored structures that can be built from them. Graphite has been the most important anode material for commercial Li-ion batteries,[4] in which Li^+ ions are reversibly inserted into and extracted from the space between the graphene layers in graphite during charge/discharge. CNTs and graphene with high specific surface areas (SSAs) can store energy by the adsorption/desorption of ions at the electrode/electrolyte interface. The energy stored is thus greatly dependent on the characteristics of the carbon material, such as its SSA,[5] pore structure, doping, and defects.[6]

Therefore, the optimization of electrochemical energy storage in carbon needs a rationally designed structure. One problem related to the use of CNTs and graphene for electrochemical energy storage is the agglomeration of the nanostructures that leads to reduced efficiency.[7] The assembly of sp^2-hybridized carbon nanostructures to form a 3D network can effectively prevent such agglomeration and thus preserve the basic structural features and electrical properties of the building blocks. In addition, the 3D network provides channels for ion migration. These two features are favored for electrochemical energy storage.[8] Following this strategy, various synthesis protocols have been developed,[9] such as the freeze-drying[10] or hydrothermal treatment[11] of graphene or CNT suspensions, and assembly with the assistance of templates.[12] With more efficient electron transfer and a more robust structure, a tailored 3D carbon will provide potentially higher electrochemical energy conversion by connecting the building blocks covalently instead of by van der Waals interactions. For example, CNTs have been welded together by ion beam irradiation at elevated temperatures.[13] A graphene foam with a SSA of ≈850 $m^2\ g^{-1}$ that was prepared by chemical vapor deposition of carbon on a nickel foam has shown an excellent electrical and mechanical characteristics for Li-ion batteries.[14]

Besides the assembly, doping and defects in the graphitic lattice play important roles in determining the electrochemical

Z. Tan, K. Ni, G. Chen, W. Zeng, Z. Tao, M. Ikram, Prof. X. Wu, Prof. H. Ji, Prof. Y. Zhu
Key Laboratory of Materials for Energy Conversion
Chinese Academy of Sciences
Department of Materials Science and Engineering
University of Science and Technology of China
96 Jin Zhai Rd, Hefei, Anhui 230026, P. R. China
E-mail: zhuyanwu@ustc.edu.cn

Q. Zhang, Prof. L. Sun
School of Electronic Science & Engineering
Southeast University
2 Sipailou, Nanjing, Jiangsu 210096, P. R. China

Dr. H. Wang
Experimental Center of Engineering and Material Sciences
University of Science and Technology of China
96 Jin Zhai Rd, Hefei, Anhui 230026, P. R. China

Prof. X. Zhu
College of Chemistry
Central China Normal University
152 Luoyu Rd, Wuhan, Hubei 430079, P. R. China

Prof. X. Wu
Hefei National Laboratory of Physical Sciences at the Microscale, and CAS Center for Excellence in Nanoscience
University of Science and Technology of China
Hefei, Anhui 230026, P. R. China

Prof. X. Wu
Synergetic Innovation of Quantum Information & Quantum Technology
University of Science and Technology of China
Hefei, Anhui 230026, P. R. China

Prof. H. Ji, Prof. Y. Zhu
iChEM (Collaborative Innovation Center of Chemistry for Energy Materials)
University of Science and Technology of China
96 Jin Zhai Rd, Hefei, Anhui 230026, P. R. China

Prof. R. S. Ruoff
Center for Multidimensional Carbon Materials (CMCM)
Institute for Basic Science (IBS)
Ulsan 689-798, South Korea
E-mail: ruofflab@gmail.com

Prof. R. S. Ruoff
Department of Chemistry and School of Materials Science
Ulsan National Institute of Science and Technology
Ulsan 689-798, South Korea

DOI: 10.1002/adma.201603414

performance of the carbon materials.[15] Nitrogen doping (N-doping) in graphene has been shown to increase the quantum capacitance of graphene and thus to increase the capacitance per unit area of the electrode/electrolyte interface.[5] It was also considered that the nitrogen atoms located at the edges of graphene layers could improve the wettability of carbon in the electrolyte; the pseudocapacitance due to faradaic redox reactions might contribute to the capacitance as well.[16] N-doped carbon materials also provide a larger number of active sites for Li-ion adsorption by increasing the number of defects through the incorporation of the nitrogen in carbon,[17] thus yielding an increased gravimetric capacity for Li-ion storage.[18] Among the three commonly observed configurations of N-dopant atoms in graphitic carbon, pyrrolic N (N5), pyridinic N (N6), and quaternary N,[19] pyrrolic N, and pyridinic N are considered to be more active for electrochemical energy storage while the graphitic structure is the weakest among them.[20] Similarly, topological defects such as divacancy and Thrower–Stone–Wales defects in the graphitic carbon may provide extra active sites for ion adsorption or for charge transfer in electrochemical energy storage.[21] In addition, numerous work has demontrated the important role of macro- and mesopores in the ion transportation for high power density or excellent rate performance in supercapacitors or Li-ion batteries.[22,23] Therefore, a carbon for superior Li-ion storage would ideally have the following features: (1) a 3D network which contains the macro or mesopores for fast ion migration; (2) a covalently connected structure made of sp^2-hybridized carbon for high electrical conductivity; and (3) a finely tuned configuration of dopant atoms and defects for more active sites.

To achieve a carbon with these features we chose a high-energy carbon nanostructure, C_{60}, which is more reactive than CNTs and graphene, as the precursor, and treated it with KOH at temperatures of 500–700 °C in an ammonia atmosphere. The processing restructured the C_{60} molecules to produce a porous carbon mainly made of sp^2-bonded carbon atoms doped with a large amount of N and containing many defects. The N-doping is dominated by pyrrolic and pyridinic nitrogen. The porous carbon with an N-doping concentration of 7.8 wt% showed a reversible specific capacity of 1900 mA h g^{-1} at a charge/discharge current density of 100 mA g^{-1} and a specific capacity of 600 mA h g^{-1} at 5 A g^{-1} when tested as the anode of a Li-ion battery. The anode was cycled for 2000 cycles at 5 A g^{-1} and a low average capacity decay rate of 0.03% per cycle was obtained. A first-principles simulation has suggested that the superior anode performance of the N-doped porous carbon is closely related to the curving of the carbon layers (graphenes) and the pyrrolic/pyridinic N-doping in the carbon.

The synthesis of activated C_{60} (aC_{60}) and N-doped aC_{60} (N-aC_{60}) samples is schematically shown in **Figure 1**a. C_{60} molecules in the powder tend to agglomerate into crystals with a face centered cubic (fcc) structure.[24] As will be shown in the following detailed characterizations, a porous carbon (aC_{60}) is obtained from Route A of the synthesis, where the normal KOH activation is performed in Ar flow. In Route B, on the other hand, N-doping occurs when an NH_3 gas flow is introduced during the annealing. As is well known, the synthesis of activated carbons includes redox reactions between carbon and KOH at temperatures of above 400 °C, followed by the creation of pores accompanied by the generation of CO_2 (g) and H_2O (g) above 700 °C and eventually potassium vapor intercalation at temperatures of above 800 °C.[25] Our recent studies have shown that the KOH reaction of microwave expanded graphite oxide performed at low temperatures (e.g., at ≈450 °C) creates nanoscale pores in the graphene platelets;[26] while a quick processing (e.g., at 600 °C for 6–8 min) of C_{60} in excess KOH (e.g., for a KOH/C_{60} ratio of 20) ruptures the C_{60} cage and leads to the preparation of carbon quantum dots.[27] In the current case, due to the lower KOH/C_{60} ratio and the longer processing time, the C_{60} fragments generated may have a much higher chance to connect to each other and assemble into a hierarchical structure at certain stage of activation, as shown in Figure 1a. In addition, it was found that the N-content increased with activation temperature in the range 500–700 °C (Figure S1a, Supporting Information) but a further temperature increase to 800 °C led to a very low yield of N-aC_{60} samples. The time at which the NH_3 was added to the gas flow showed a minor influence on the N-content, as indicated in Figure S1b (Supporting Information).

Typical scanning electron microscopy (SEM) and transmission electron microscopy (TEM) images of aC_{60} are shown in Figure 1b–d. As we can see, aC_{60} has a sponge-like structure with hierarchical pores with sizes from a few to several hundred nanometers. The electron diffraction (ED) pattern of aC_{60} features faint rings, indicating that aC_{60} is dominated by an amorphous structure, in contrast to the well-crystallized structure of the C_{60} precursor (Figure S2c,d, Supporting Information). Characteristic lattice spacings of 0.126 and 0.217 nm have been estimated from the ED pattern of aC_{60}, and these are close to the in-plane lattice spacings of 0.123 nm (110) and 0.214 nm (100) of graphene (JCPDS File 41-1487), respectively.[28] From the high resolution transmission electron microscopy (HRTEM) image in Figure 1d, we can see that the walls of hierarchical aC_{60} are composed of curved layers with an average interlayer spacing of about 0.474 nm (inset of Figure 1d), significantly larger than the interlayer distance in graphite (0.335 nm).[29] N-aC_{60} samples, e.g., N7.5%-aC_{60} with a N-content of 7.5 wt%, have a porous structure similar to aC_{60} as seen from the SEM and TEM images in Figure 1e and in Figure S2a,b (Supporting Information). Lattice spacings of 0.124 and 0.231 nm were estimated from the ED pattern (inset of Figure S2b, Supporting Information). Energy dispersive spectrometer (EDS) elemental mapping performed on N7.5%-aC_{60} shows that elemental C (Figure 1f) and N (Figure 1g) are uniformly distributed, indicating efficient N-doping in the 3D carbon structure through KOH activation of the C_{60} molecules in NH_3. Aberration-corrected TEM images of the N-aC_{60} (e.g., N7.8%-aC_{60}) are shown in Figure S2e,f (Supporting Information). From the atomic-resolution images we can find many curvatures from the carbon, as indicated by the high contrast and the large amount of topological defects such as pentagons and heptagons.

X-ray diffraction (XRD) diffractograms of C_{60}, aC_{60}, and N7.5%-aC_{60} are shown in **Figure 2**a. The characteristic peaks corresponding to diffraction from C_{60} crystals (fcc) have been labeled.[30] As a result of the activation, all these peaks totally vanished in the patterns from aC_{60} and N7.5%-aC_{60}, indicating that the C_{60} crystals have been completely restructured by KOH activation. The wide peaks at 24.3° and 43.2° in aC_{60} can be respectively attributed to (002) and (100) diffraction in graphitic

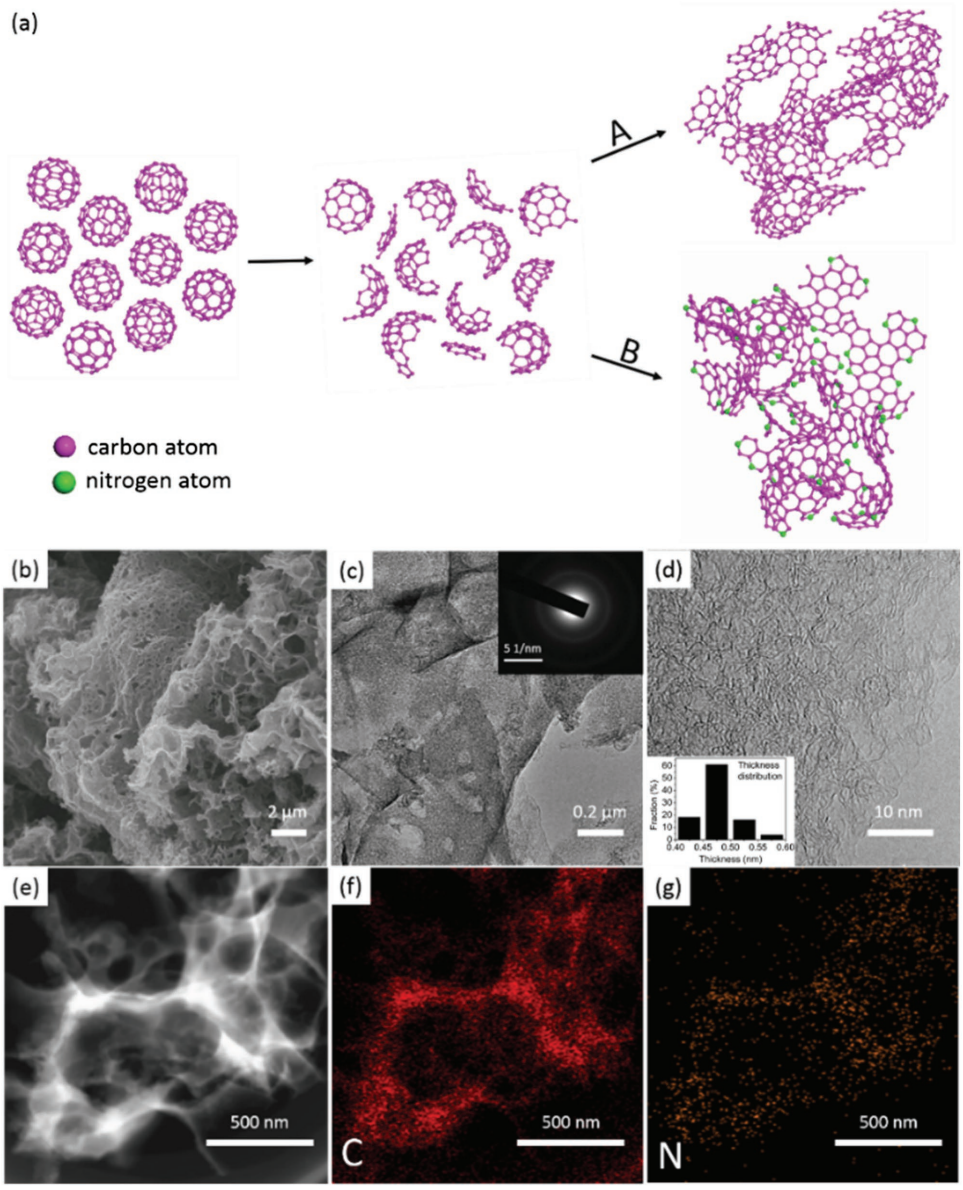

Figure 1. a) Schematic of KOH activation of C_{60} molecules. Route A indicates the normal activation performed in an Ar flow while Route B shows N-doping when NH_3 flow is involved in the activation. Hydrogen and oxygen atoms are not shown. b) Typical SEM image of aC_{60}. c) Typical TEM image of aC_{60}, with an electron diffraction pattern in the inset. d) TEM image of aC_{60} at a higher magnification with the inset showing the distribution of the interlayer spacings. e) Typical TEM image of N7.5%-aC_{60} and f,g) corresponding EDS maps of elemental C (f) and N (g).

carbon. With N-doping, the position of (002) diffraction peak remains at 24.6° (corresponding to a spacing of ≈0.362 nm). Note that the low-angle scattering in the XRD patterns of aC_{60} and N7.5%-aC_{60} is much higher than for C_{60}, consistent with the presence of a high volume of pores in the activated samples. From the Raman spectrum of C_{60} shown in Figure 2b, the characteristic peaks of C_{60} such as Hg (eight fivefold-degenerated modes of symmetry) and Ag (two nondegenerate modes of symmetry) can be identified.[31] After activation, all these features disappear; instead, two bands commonly observed in graphitic carbons, namely the D- and G-bands at 1348 and 1585 cm^{-1}, respectively,[31] are observed from aC_{60} and N7.5%-aC_{60}. The relatively high plateau between the D- and G-bands might be related to the possibly remaining pentagons[32] in the activated C_{60}, as observed in some positions shown in Figure S2f (Supporting Information). The intensity ratios of the D- to G- bands are 0.90 and 0.95 for aC_{60} and N7.5%-aC_{60}, respectively, suggesting slightly more defects in N7.5%-aC_{60}. Figure 2c shows Fourier transform infrared spectroscopy (FTIR) spectra for C_{60}, aC_{60}, and N7.5%-aC_{60}. The valleys at 527, 576, 1183, and 1428 cm^{-1} in the C_{60} spectrum result from four infrared active modes with F_{1u} symmetry, associated with the primarily radial motion of carbon atoms (527 and 576 cm^{-1}) and the tangential motion of carbon atoms (1182 and 1427 cm^{-1}) in C_{60}.[33] All these vibrations disappear in aC_{60} and N7.5%-aC_{60}, except for the modes at 1637, 2910, and 3453 cm^{-1}, which are attributed

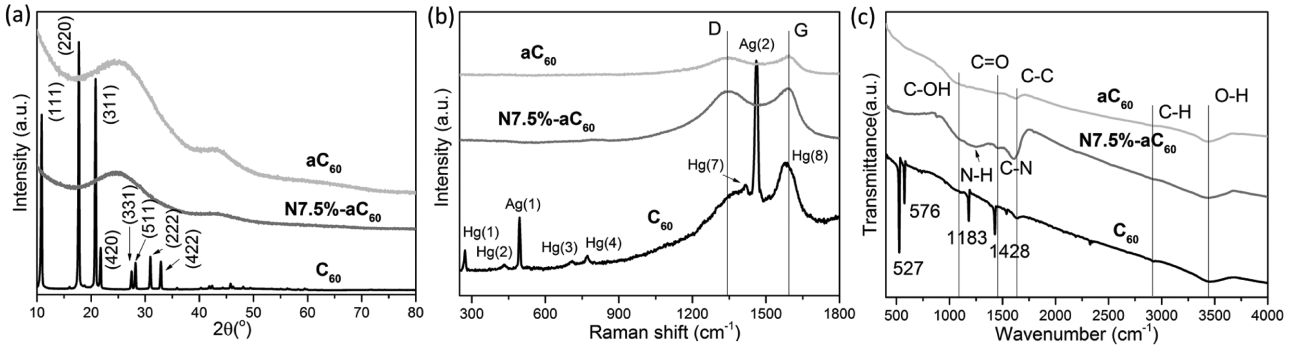

Figure 2. a) XRD diffractograms of C_{60}, aC_{60}, and N7.5%-aC_{60}. b) Raman spectra of C_{60}, aC_{60}, and N7.5%-aC_{60}. c) FTIR spectra of C_{60}, aC_{60}, and N7.5%-aC_{60}.

to π–π interaction, C—H stretching and O—H stretching, respectively. The broad modes at 1092 and 1455 cm^{-1} in aC_{60} and N7.5%-aC_{60} are respectively due to hydrogen-containing groups, such as C—OH stretching, and C=O stretching in the carboxylic group. With N-doping, extra modes at 1244 and 1605 cm^{-1} are observed in N7.5%-aC_{60}, corresponding to N—H and C=N bond stretching, respectively.[34] These results clearly show that the cages of aC_{60} are completely ruptured and graphitic carbons with no sign of any C_{60} molecules are obtained by the KOH activation. The processing has also introduced oxygen-containing groups, and N-doping when NH_3 was added during the annealing.

X-ray photoelectron spectroscopy (XPS) has been used to investigate the details of the chemical doping in the 3D carbons and survey and C 1s spectra of C_{60}, aC_{60}, and N7.5%-aC_{60} are shown in Figure S3 (Supporting Information). The C 1s peak is mainly due to sp^2 carbon bonding for all samples. Among them, the C 1s peak (284.6 eV) for C_{60} is typical of sp^2 carbon with a monopole-like electron transition across the highest occupied molecular orbital–lowest unoccupied molecular orbital gap and a dipole-like π–π^* shake-up satellite.[35] Consistent with the FTIR results, peaks attributed to C—OH and C=O bonds are observed in the C 1s spectra of both aC_{60} and N7.5%-aC_{60}. Estimations using the XPS data show that oxygen content increases from 1.3 at.% in C_{60} to 4.2 at.% in aC_{60} and to 9.5 at.% in N7.5%-aC_{60}.

On the other hand, a nitrogen peak, which is absent in the spectra from C_{60} and aC_{60}, can be clearly observed in the survey spectrum of N7.5%-aC_{60}. The N-content estimated from combustion elemental analysis is roughly consistent with that obtained from XPS (Table S1, Supporting Information) considering the measurement error and difference in techniques. The detailed XPS N 1s spectrum of N7.5%-aC_{60} is shown in **Figure 3**a, in which the prominent band can be deconvoluted into two peaks, namely pyrrolic N (399.8 ± 0.2 eV) and pyridinic N (398.4 ± 0.2 eV). Pyrrolic N or N5 represents the nitrogen atoms in a five-membered ring and thus contributing two electrons to the π system; pyridinic N or N6 indicates the doping where a nitrogen atom substitutes for a carbon atom in a hexagon.[36] In contrast to graphitic N that is formed by substituting a carbon atom in a complete 2D honeycomb lattice, N5 or N6 is accompanied by defects in the graphene, as shown in the schematic in Figure 3a. N5 contributes to 86.5% of the N-doping in N7.5%-aC_{60}, which may be related to the existence of pentagons in the C_{60} precursor. The dominance of N5 and N6 doping instead of graphitic N doping in N7.5%-aC_{60} can be attributed to the highly defective 3D assembly generated during the reaction with KOH. Electron spin resonance (ESR) results for aC_{60} and N7.5%-aC_{60} are shown in Figure 3b. Based on an estimation using DPPH (2,2-diphenyl-1-picrylhydrazyl) as reference, the concentration of spins is 7.44×10^{18} spins g^{-1} for N7.5%-aC_{60} and 1.06×10^{16} spins g^{-1} for aC_{60}, both higher than that from C_{60}.[37] With nitrogen doping, a significant broadening of the resonance is observed in N7.5%-aC_{60} and this could be indicative of hyperfine interactions in the sources, weak magnetic interactions between the spin of unpaired electrons and nuclear spin,[38] which may be magnified by the extra electron energy levels caused by N-doping.

High-resolution N_2 adsorption/desorption isotherms performed at 77.4 K are shown in Figure 3c. The hysteresis loops of both aC_{60} and N7.5%-aC_{60} demonstrate a type H4 feature (as classified by the International Union of Pure and Applied Chemistry (IUPAC)) which is generally observed in materials containing both micropores and mesopores.[39] The higher isotherm of aC_{60} in the low-pressure region where micropore filling occurs, suggests that aC_{60} has more micropores than N7.5%-aC_{60}. Brunauer-Emmett-Teller SSAs of aC_{60} and N7.5%-aC_{60}, calculated from the linear range of the isotherms, are 1457 and 1274 $m^2\ g^{-1}$, respectively, much higher than that of C_{60} (8.15 $m^2\ g^{-1}$) while similar to that of the porous carbon obtained from C_{70} microtubes (1249 $m^2\ g^{-1}$).[40] Figure 3d shows the cumulative pore volumes and pore size distributions by applying a hybrid nonlocal density functional theory (NLDFT) kernel, assuming a slit pore geometry for the micropores and a cylindrical pore geometry for the mesopores. The pore volumes of aC_{60} and N7.5%-aC_{60} are respectively measured as 0.895 and 1.02 $cm^3\ g^{-1}$, significantly higher than 0.007 $cm^3\ g^{-1}$ for C_{60} powder, and consistent with the indications from XRD results referred to earlier. The pore size distributions (inset of Figure 3d) show that both aC_{60} and N7.5%-aC_{60} have a high micropore volume with size smaller than 0.8 nm, while N7.5%-aC_{60} has a more prominent size distribution centered at around 1.5 nm. Figure 3d suggests that the higher pore volume of N7.5%-aC_{60} is attributed to pores bigger than 5 nm, which is consistent to the relatively lower fraction of micropores in N7.5%-aC_{60} (29.4%, compared to 52.5% in aC_{60}, as seen in Table S2, Supporting Information), although the NLDFT model did not give the analysis across the whole mesopore size range from 2 to 50 nm.

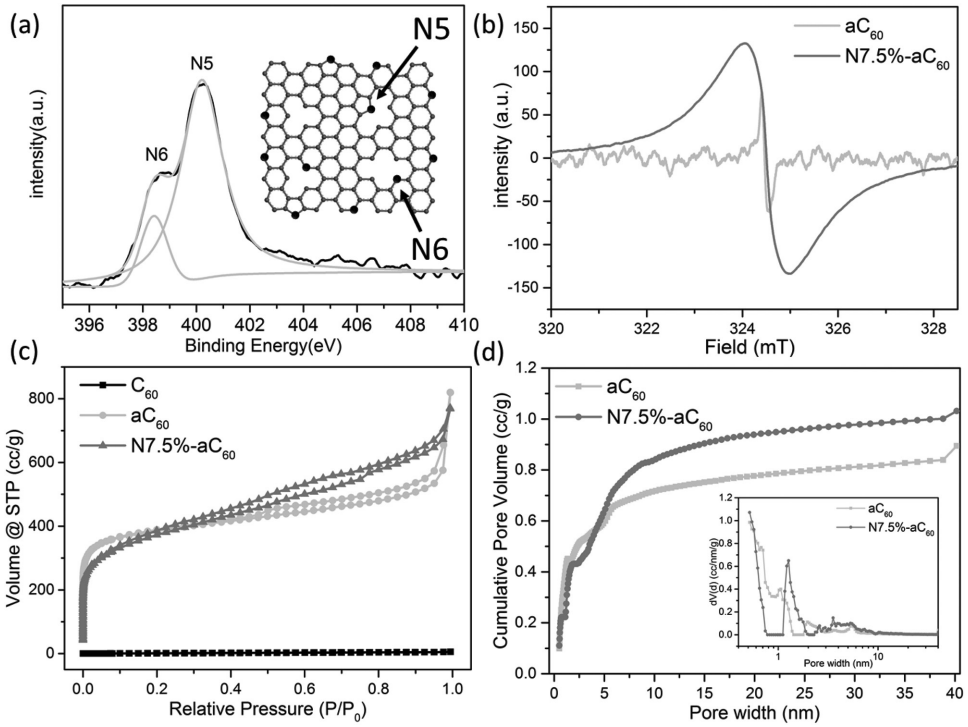

Figure 3. a) XPS N1s spectrum of N7.5%-aC_{60}. b) ESR spectra of N7.5%-aC_{60} and aC_{60}. c) High-resolution, low-pressure N_2 isotherms of C_{60}, aC_{60}, and N7.5%-aC_{60}. d) Cumulative pore volume and (inset) pore-size distribution of aC_{60} and N7.5%-aC_{60}, calculated using a slit/cylinder NLDFT model.

Figure 4a shows typical cyclic voltammetry curves of N7.5%-aC_{60} in a half-cell with a 1 M $LiPF_6$ in ethylene carbonate/diethyl carbonate (EC/DEC) electrolyte at a scan rate of 0.1 mV s^{-1}. A pronounced cathodic peak at around 0.7 V in the 1st cycle is observed, which can be attributed to the formation of a solid electrolyte interphase (SEI) layer on the surface of the electrode

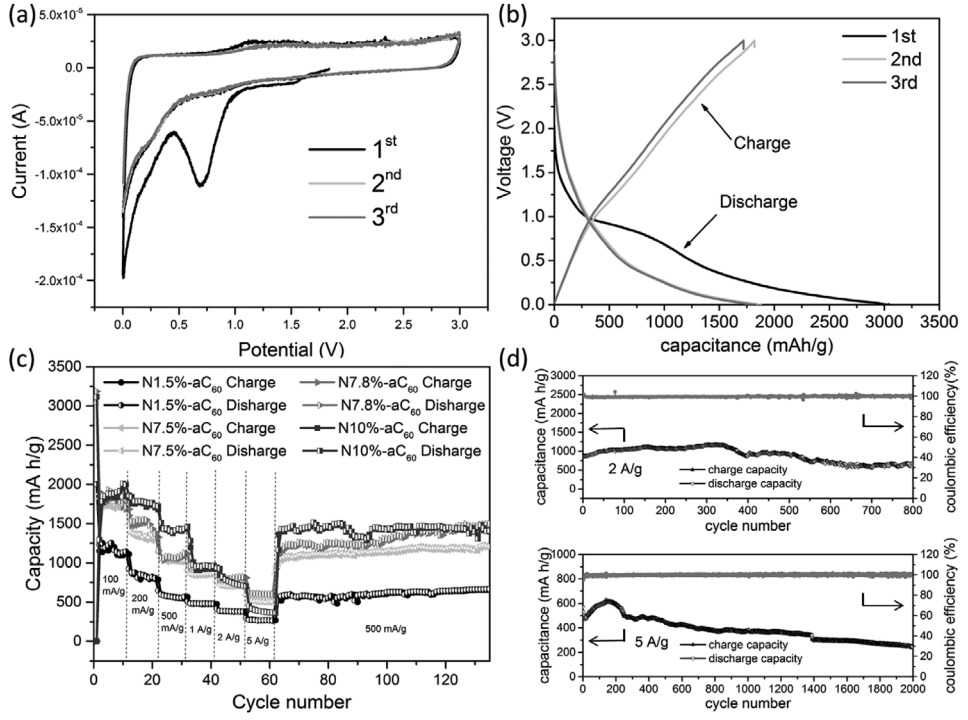

Figure 4. a) Cyclic voltammogram at 0.1 mV s^{-1} and b) galvanostatic charge–discharge profiles at a current of 100 mA g^{-1} for N7.5%-aC_{60} in a half-cell with 1 M $LiPF_6$ in EC/DEC electrolyte. c) Rate performance of N1.5%-aC_{60}, N7.5%-aC_{60}, N7.8%-aC_{60}, and N10%-aC_{60}. d) Cycling performance of N7.8%-aC_{60} at current density of 2 and 5 A g^{-1}.

material because of electrolyte decomposition and the formation of lithium organic compounds.[41] The intensity of this peak is remarkably reduced in the following cycles, indicating the occurrence of irreversible reactions.[42] Figure 4b shows the discharge/charge profiles of the first three cycles for N7.5%-aC_{60} at a current of 100 mA g^{-1} between 0.01 and 3.0 V. A plateau observed at ≈0.9 V in the first cycle shown in Figure 4b corresponds to the formation of an SEI layer.[42] An initial capacity of 3040 mA h g^{-1} is obtained from the discharge curve in the first cycle for N7.5%-aC_{60}, while the first charge curve gives a capacity of 1820 mA h g^{-1}, resulting in an initial Coulombic efficiency of ≈60%. After the second cycle, a reversible specific capacity of 1878 mA h g^{-1} is obtained with a Coulombic efficiency of nearly 100%. Figure 4c shows the rate performance of N-aC_{60} electrodes, for which the cells were cycled at each rate for 10 cycles until a rate of 5 A g^{-1} was obtained, then back to the current density of 500 mA g^{-1} for 65 cycles. An excellent rate capability, e.g., indicated by capacities of 1030 mA h g^{-1} at 500 mA g^{-1} and 856 mA h g^{-1} at 1 A g^{-1}, is obtained from the N7.5%-aC_{60} anode. Note that with a similar N-doping level, N7.8%-aC_{60} shows a reversible capacity of 1903 mA h g^{-1} at 100 mA g^{-1}, close to that for N7.5%-aC_{60}, but capacities higher than those for N7.5%-aC_{60} at currents of 2 A g^{-1} (≈800 mA h g^{-1}) and 5 A g^{-1} (≈600 mA h g^{-1}), as well as when the current goes back to 500 mA g^{-1} at the end of rate-performance measurements. For a significantly lower N-doping, e.g., in the case of N1.5%-aC_{60}, the capacities at all rates are lower, but still show a reversible capacity of 1200 mAh g^{-1} at 100 mA g^{-1}. When the N-content is further increased to about 10 wt% in N10%-aC_{60}, the reversible capacity shows a slightly lower value of 1835 mA h g^{-1} at the beginning of cycling at 100 mA g^{-1}, then increases to about 2000 mA h g^{-1} and remains at high values for small currents, e.g., 200 mA g^{-1} (1780 mA h g^{-1}) and 500 mA g^{-1} (1420 mA h g^{-1}). However, the capacity of N10%-aC_{60} drops remarkably at 5 A g^{-1}. N7.8%-aC_{60} has the most balanced capacity and rate performance among the N-aC_{60} samples studied and was thus used for cycling capability measurements.

Figure 4d shows the cycling stability of N7.8%-aC_{60} at 2 and 5 A g^{-1}. The initial cycling at 2 A g^{-1} shows an increase in the capacity, to a value of about 1200 mA h g^{-1} after 300 cycles, which could be explained by the further development of an SEI layer and/or a reaction between carbon and the electrolyte.[43] After that the capacity shows a constant decrease until around the 700th cycle and then remains stable at 600 mA h g^{-1} until the 800th cycle. At a current of 5 A g^{-1}, the capacity also shows an increase to above 600 mA h g^{-1} and then a steady decrease to about 300 mA h g^{-1} after 2000 cycles. Both measurements have demonstrated a Coulombic efficiency of nearly 100%, regardless of capacity. To investigate the change in the electrode after electrochemical tests, the morphology of N7.8%-aC_{60} before and after the first cycle of anode measurement was compared and the TEM images are shown in Figure S4 (Supporting Information). It can be seen that the original N7.8%-aC_{60} (Figure S4a, Supporting Information) has been covered by an amorphous layer after the first cycle of testing (Figure S4b, Supporting Information). The further study on the material srcatched from the electrode indicated that the amorphous layer is not uniform in the sample, as shown in the TEM images in Figure S5 (Supporting Information). From the corresponding EDS spectra (Figure S5, Supporting Information), the presence of nitrogen can be detected from some areas but not from other areas especially for those with the amorphous coating. However, because of the complicated situation in the carbon electrode after the testing, it is challenging to figure out the exact change in the chemical component of the N-aC_{60} electrode. In general, N7.8%-aC_{60} has shown one of the best anode performances, in terms of specific capacity, rate capability, and cycling stability, compared to those of N-doped carbons, as summarized in Table S3 (Supporting Information). In addition, the performance of N7.8%-aC_{60} shows a weak dependence of poly(vinylidene fluoride) (PVDF) content in the electrode for the conditions studied, as shown in Figure S6 (Supporting Information). The similar or even slightly better rate performance for electrodes made with a lower PVDF content suggests that the practical capacity of N-aC_{60} anodes could reach a higher value with a higher amount of active material in the electrodes after further optimization.

To further understand the mechanisms for the superior of Li-ion storage ability, we investigated the adsorption behavior of Li atoms on graphene and C_{60} fragments with and without nitrogen doping through molecular modeling. Two possible effects, i.e., a curvature effect and a N-doping effect, have been considered. For the former, we compared the adsorption energy of a Li atom on half a C_{60} molecule with edges saturated by H, i.e., $C_{30}H_{10}$, and a flat graphene fragment containing the same number of carbon atoms, i.e., $C_{30}H_{14}$. Various adsorption sites were tested and are shown in Figure S7a,b (Supporting Information). As shown in **Figure 5**a, the center of the inner side of bowl-like $C_{30}H_{10}$ has the largest adsorption energy for a Li atom of −2.51 eV calculated using the DFT-D2 method. This value is larger than that obtained on a flat graphene fragment (shown in Figure 5b), which is about −1.88 eV at the same calculation accuracy. In contrast, the adsorption energy for a Li atom on perfect graphene is −1.64 eV (Figure S7c, Supporting

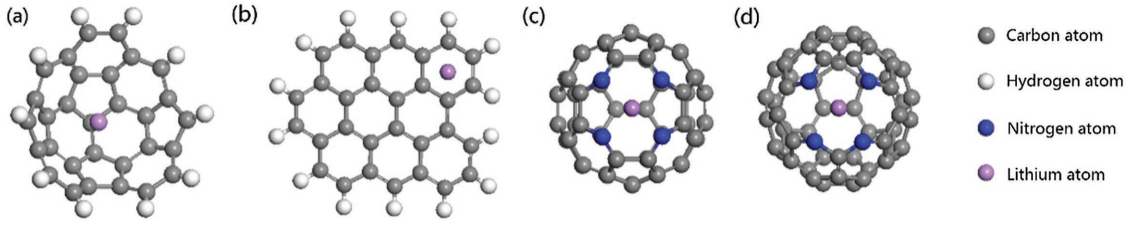

Figure 5. Optimized structures of a) a bowl-like $C_{30}H_{10}$ molecule with a single Li atom adsorbed on the inner side, b) a flat $C_{30}H_{14}$ molecule with a single Li atom adsorption, c) a $C_{54}N_4$ molecule with a single Li atom adsorbed between four N6 atoms, and d) a $C_{54}N_4$ molecule with a single Li atom adsorbed between two N6 atoms and two N5 atoms.

Information), indicating that the edge affects the adsorption of Li atoms on small or defective graphene fragments. The results have clearly shown that introducing curvature can efficiently increase the adsorption of Li atoms on carbon materials.

For the doping effect, two types of doped nitrogen atoms, i.e., N5 and N6 nitrogen in a C_{60} molecule were considered. To simplify the calculations and to eliminate the edge effect, a $C_{54}N_4$ molecule with 4 nitrogen atoms replacing carbon atoms in a C_{58} molecule, obtained from removing two carbon atoms from a pristine C_{60} molecule, was considered. The N-doping concentration in such a model is about 8 wt.%, consistent with that in the N-aC_{60} samples with optimum Li-ion anode performance. As shown in Figure 5c,d, two arrangements of nitrogen atoms in the $C_{54}N_4$ molecule were adopted, e.g., forming four N5 nitrogen atoms or two N5 and two N6 nitrogen atoms in the framework of a $C_{54}N_4$ molecule. This is similar to what has been used in a simulation for N-doped graphene.[21] When a Li atom is adsorbed at the center of defects in both models, the adsorption energy is calculated as –5.56 eV for four N5 nitrogen atoms or –6.03 eV for two N5 and two N6 nitrogen atoms. Such adsorption energy values are remarkably higher than those on the outer or the inner sides of a pristine C_{60} molecule, which were respectively calculated as –2.31 or –2.41 eV using the same computational configuration. These results indicate that N-doping, especially N5 nitrogen, can improve the adsorption ability for Li in the $C_{54}N_4$ structure. Several other models have also been considered and discussed in order to make a comparison between N-doping in defective C_{60} molecules and in defective graphene. The results (Figure S8, Supporting Information) have pointed to the conclusion that the Li adsorption energy for N5 doping in defective C_{60} is generally larger than that for the same doping in graphene, while the Li adsorption for N6 doping is comparable in both systems. The simulation results about the effect of N-doping roughly explained the anode performances shown above, especially by comparing the nitrogen and oxygen contents in different samples, as shown in Table S1 (Supporting Information).

Besides the superior performance as an anode in Li-ion batteries, N-aC_{60} and a-C_{60} have also shown fairly good performance as electrodes for supercapacitors. A two-electrode symmetrical supercapacitor measurement with aC_{60} as the electrode has given a specific capacitance of 118 F g^{-1} at a current density of 0.2 A g^{-1} in a 1-butyl-3-methylimidazolium tetrafluoroborate in acetonitrile (BMIM BF_4/AN) electrolyte (Figure S9, Supporting Information). The ESR of the test cell based on aC_{60} is 2.3 Ω. With N-doping, the supercapacitor performance of N-aC_{60} samples shows a dependence on N-content, as shown in Figure S9e,f (Supporting Information). When the N-content is increased from 1.5 to 6.4 wt%, the specific capacitance increases from 38.2 to 114.6 F g^{-1} at a constant current of 1 A g^{-1} in BMIM PF_6/AN. A further increase of the N-content to 9.6 wt% led to a slightly lower specific capacitance of 107 F g^{-1} under the same measurement conditions. The similar supercapacitor performances of aC_{60} and N6.4%-aC_{60} observed in the current work could be explained by the balance between pore structure and the doping effect. Although N-doping has been considered to increase the quantum capacitance in very thin graphene-like layers,[44] the lower volume of micropores in N-aC_{60} compared to aC_{60} may decrease the capacitance at the same time.[45] In comparison, the nanoporous carbon obtained by heating tubular assembly C_{60} at 2000 °C in vacuum showed a specific capacitance of up to 145.5 F g^{-1} measured at a scan rate of 5 mV s^{-1} in a three-electrode system in 1 M H_2SO_4.[46] A higher specific capacitance of 362.0 F g^{-1} measured at 0.1 A g^{-1} in a three-electrode system in 1 M H_2SO_4 was obtained from the porous carbon by treating tubular assembly of C_{70} with KOH activation.[45] The N-doping configuration in activated fullerenes may need further optimization to improve the supercapacitor performance, as shown in the comparison in Table S4 (Supporting Information).

In summary, KOH activation in ammonia has been used to completely convert C_{60} molecules to a 3D porous carbon while simultaneously doping with pyridinic and pyrrolic nitrogen. The N-doping also caused more defects and a higher volume of meso and macropores in the carbon. By controlling the activation process, the doping level could be optimized (around 7.5%–7.8% for the anode), leading to a highly reversible capacity of about 1900 mA h g^{-1} at a current of 100 mA g^{-1} as an anode for Li-ion batteries. An outstanding rate performance (e.g., 800 mA h g^{-1} at 2 A g^{-1} and 600 mA h g^{-1} at 5 A g^{-1}) and an excellent cycling stability (e.g., 600 mA h g^{-1} after 800 cycles at 2 A g^{-1} and 300 mA h g^{-1} after 2000 cycles at 5 A g^{-1}) have been demonstrated. Simulations show that the curved layer structure and N-doping, especially pyrrolic nitrogen, have contributed to the high Li-ion storage capacity in the carbon.

Supporting Information

Supporting Information is available from the Wiley Online Library or from the author.

Acknowledgements

Z.T. and K.N. contributed equally to this work. Y.Z. appreciates financial support from the China Government 1000 Plan Talent Program, China MOE NCET Program, Natural Science Foundation of China (Grant No. 51322204), the Fundamental Research Funds for the Central Universities (Grant Nos. WK2060140014 and WK2060140017), and funding from the Hefei National Synchrotron Radiation Lab. X.W. was supported by the NSFC (Grant Nos. 21421063, 51172223, and 21573204), by the Strategic Priority Research Program of CAS (Grant No. XDB01020300), the Fundamental Research Funds for the Central Universities (Grant Nos. WK2060190025 and WK2310000053), by the National Key Basic Research Program (Grant No. 2012CB922001), by the National Program for Support of Top-notch Young Professional, the External Cooperation Program of BIC of CAS (Grant No. 211134KYSB20130017), and by USTCSCC, SCCAS, Tianjin, and Shanghai Supercomputer Centers. R.S.R. acknowledges support from the Institute for Basic Science (Grant No. IBS-R019-D1).

Received: June 28, 2016
Revised: September 10, 2016
Published online:

[1] H. W. Kroto, J. R. Heath, S. C. O'Brien, R. F. Curl, R. E. Smalley, *Nature* **1985**, *318*, 162.
[2] S. Iijima, *Nature* **1991**, *354*, 56.

[3] K. S. Novoselov, D. Jiang, F. Schedin, T. J. Booth, V. V. Khotkevich, S. V. Morozov, A. K. Geim, *Proc. Natl. Acad. Sci. USA* **2005**, *102*, 10451.
[4] H. Shi, J. Barker, M. Y. Saidi, R. Koksbang, *J. Electrochem. Soc.* **1996**, *143*, 3466.
[5] H. Ji, X. Zhao, Z. Qiao, J. Jung, Y. Zhu, Y. Lu, L. L. Zhang, A. H. MacDonald, R. S. Ruoff, *Nat. Commun.* **2014**, *5*, 3317.
[6] G. Luo, L. Liu, J. Zhang, G. Li, B. Wang, J. Zhao, *ACS Appl. Mater. Interfaces* **2013**, *5*, 11184.
[7] a) Z. Yang, J. Ren, Z. Zhang, X. Chen, G. Guan, L. Qiu, Y. Zhang, H. Peng, *Chem. Rev.* **2015**, *115*, 5159; b) Q. Wang, J. Yan, Z. J. Fan, *Energy Environ. Sci.* **2016**, *9*, 729.
[8] A. S. Arico, P. Bruce, B. Scrosati, J. M. Tarascon, W. van Schalkwijk, *Nat. Mater.* **2005**, *4*, 366.
[9] a) M. H. Yu, W. T. Qiu, F. X. Wang, T. Zhai, P. P. Fang, X. H. Lu, Y. X. Tong, *J. Mater. Chem. A* **2015**, *3*, 15792; b) Q. L. Fang, Y. Shen, B. L. Chen, *Chem. Eng. J.* **2015**, *264*, 753.
[10] D. D. Cai, S. Q. Wang, L. X. Ding, P. C. Lian, S. Q. Zhang, F. Peng, H. H. Wang, *J. Power Sources* **2014**, *254*, 198.
[11] Y. Xu, K. Sheng, C. Li, G. Shi, *ACS Nano* **2010**, *4*, 4324.
[12] G. L. Che, B. B. Lakshmi, E. R. Fisher, C. R. Martin, *Nature* **1998**, *393*, 346.
[13] Z. C. Ni, Q. T. Li, L. Yan, J. L. Gong, D. Z. Zhu, *Carbon* **2008**, *46*, 376.
[14] Z. Chen, W. Ren, L. Gao, B. Liu, S. Pei, H. M. Cheng, *Nat. Mater.* **2011**, *10*, 424.
[15] K. N. Wood, R. O'Hayre, S. Pylypenko, *Energy Environ. Sci.* **2014**, *7*, 1212.
[16] G. Lota, B. Grzyb, H. Machnikowska, J. Machnikowski, E. Frackowiak, *Chem. Phys. Lett.* **2005**, *404*, 53.
[17] J. Hou, C. Cao, F. Idrees, X. Ma, *ACS Nano* **2015**, *9*, 2556.
[18] H. B. Wang, C. J. Zhang, Z. H. Liu, L. Wang, P. X. Han, H. X. Xu, K. J. Zhang, S. M. Dong, J. H. Yao, G. L. Cui, *J. Mater. Chem.* **2011**, *21*, 5430.
[19] R. Arenal, K. March, C. P. Ewels, X. Rocquefelte, M. Kociak, A. Loiseau, O. Stephan, *Nano Lett.* **2014**, *14*, 5509.
[20] C. C. Ma, X. H. Shao, D. P. Cao, *J. Mater. Chem.* **2012**, *22*, 8911.
[21] L. J. Zhou, Z. F. Hou, L. M. Wu, *J. Phys. Chem. C* **2012**, *116*, 21780.
[22] S. Murali, N. Quarles, L. L. Zhang, J. R. Potts, Z. Tan, Y. Lu, Y. Zhu, R. S. Ruoff, *Nano Energy* **2013**, *2*, 764.
[23] K. T. Lee, J. C. Lytle, N. S. Ergang, S. M. Oh, A. Stein, *Adv. Funct. Mater.* **2005**, *15*, 547.
[24] a) Y. J. Guo, N. Karasawa, W. A. Goddard, *Nature* **1991**, *351*, 464; b) W. I. F. David, R. M. Ibberson, J. C. Matthewman, K. Prassides, T. J. S. Dennis, J. P. Hare, H. W. Kroto, R. Taylor, D. R. M. Walton, *Nature* **1991**, *353*, 147.
[25] J. Wang, S. Kaskel, *J. Mater. Chem.* **2012**, *22*, 23710.
[26] S. Wu, G. Chen, N. Y. Kim, K. Ni, W. Zeng, Y. Zhao, Z. Tao, H. Ji, Z. Lee, Y. Zhu, *Small* **2016**, *12*, 2376.
[27] G. Chen, S. Wu, L. Hui, Y. Zhao, J. Ye, Z. Tan, W. Zeng, Z. Tao, L. Yang, Y. Zhu, *Sci. Rep.* **2016**, *6*, 19028.
[28] G. X. Wang, J. Yang, J. Park, X. L. Gou, B. Wang, H. Liu, J. Yao, *J. Phys. Chem. C* **2008**, *112*, 8192.
[29] a) J. C. Scanlon, L. B. Ebert, *J. Phys. Chem.* **1993**, *97*, 7138; b) W. Kratschmer, L. D. Lamb, K. Fostiropoulos, D. R. Huffman, *Nature* **1990**, *347*, 354.
[30] K. Zhang, Y. Zhang, S. Wang, *Sci. Rep.* **2013**, *3*, 3448.
[31] H. Kuzmany, R. Pfeiffer, M. Hulman, C. Kramberger, *Philos. Trans. A Math. Phys. Eng. Sci.* **2004**, *362*, 2375.
[32] L. Wang, B. Liu, H. Li, W. Yang, Y. Ding, S. V. Sinogeikin, Y. Meng, Z. Liu, X. C. Zeng, W. L. Mao, *Science* **2012**, *337*, 825.
[33] H. Kuzmany, R. Winkler, T. Pichler, *J. Phys.: Condens. Matter* **1995**, *7*, 6601.
[34] Y. Mao, H. Duan, B. Xu, L. Zhang, Y. S. Hu, C. C. Zhao, Z. X. Wang, L. Q. Chen, Y. S. Yang, *Energy Environ. Sci.* **2012**, *5*, 7950.
[35] J. A. Leiro, M. H. Heinonen, T. Laiho, I. G. Batirev, *J. Electron. Spectrosc.* **2003**, *128*, 205.
[36] W. Ren, D. J. Li, H. Liu, R. Mi, Y. Zhang, L. Dong, L. Dong, *Electrochim. Acta* **2013**, *105*, 75.
[37] G. X. Chen, Z. W. Zhuo, K. Ni, N. Y. Kim, Y. Zhao, Z. W. Chen, B. Xiang, L. H. Yang, Q. Zhang, Z. Lee, X. J. Wu, R. S. Ruoff, Y. W. Zhu, *Small* **2015**, *11*, 5296.
[38] S. S. Rao, A. Stesmans, J. van Tol, D. V. Kosynkin, A. Higginbotham-Duque, W. Lu, A. Sinitskii, J. M. Tour, *ACS Nano* **2012**, *6*, 7615.
[39] J. C. Groen, L. A. A. Peffer, J. Perez-Ramirez, *Microporous Mesoporous Mater.* **2003**, *60*, 1.
[40] S. Zheng, H. Ju, X. Lu, *Adv. Energy Mater.* **2015**, *5*, 1500871.
[41] Z. Li, Z. W. Xu, X. H. Tan, H. L. Wang, C. M. B. Holt, T. Stephenson, B. C. Olsen, D. Mitlin, *Energy Environ. Sci.* **2013**, *6*, 871.
[42] F. Zheng, Y. Yang, Q. Chen, *Nat. Commun.* **2014**, *5*, 5261.
[43] L. Qie, W. M. Chen, Z. H. Wang, Q. G. Shao, X. Li, L. X. Yuan, X. L. Hu, W. X. Zhang, Y. H. Huang, *Adv. Mater.* **2012**, *24*, 2047.
[44] N. A. Kumar, J. B. Baek, *Nanotechnology* **2015**, *26*, 492001.
[45] P. Simon, Y. Gogotsi, *Nat. Mater.* **2008**, *7*, 845.
[46] L. Li, A. R. Raji, J. M. Tour, *Adv. Mater.* **2013**, *25*, 6298.